EFFECT OF THE LASER POLARIZATION ON ELECTRON ACCELERATION IN CARBON NANOTUBE TARGETS*

B.S. Nunes†, N.D. Vieira Junior, R.E. Samad, Nuclear and Energy Research Institute, São Paulo, Brazil
A. Bonatto, M.S. Alva-Sánchez, Universidade Federal de Ciências da Saúde de Porto Alegre, Porto Alegre, Brazil
B. Lei, C. Bonţoiu, University of Liverpool, Liverpool, United Kingdom
G. Xia, University of Manchester, Manchester, United Kingdom
J. Resta-López, Instituto Universitario de Ciencia de los Materiales, Valencia, Spain

Abstract

Structured carbon-nanotube targets can be used as a medium for accelerating self-injected electrons within a laser-driven wakefield bubble, analogous to blowout laser wakefield acceleration (LWFA) in gaseous plasmas. A previous numerical work demonstrated this behavior using a three-cycle, 800 nm, circularly polarized laser pulse with a peak power of 35.5 TW. Here, we compare electron beam properties for linearly and circularly polarized pulses interacting with a similar target. We found that circular polarization increases the charge of electrons above 20 MeV by approximately 9%, while average energy, energy spread, emittance, and divergence remain comparable between the two polarization states.

INTRODUCTION

Over the past few decades, plasma-based accelerators [1] have emerged as a promising approach for electron acceleration using either ultraintense laser pulses—known as laser wakefield acceleration (LWFA) [2, 3]—or charged particle beams, called beam-driven wakefield acceleration (PWFA) [4]. In these schemes, the driver propagates through an ionized gas, typically generated by gas jets or capillary discharge cells, exciting large-amplitude wakefields by perturbing the local electron density. These wakefields can sustain accelerating gradients on the order of several GeV/m, enabling the production of high-quality electron bunches for a wide range of applications, including medical radioisotope production [5], radiotherapy [6], industrial applications [7], and high-energy physics research [8, 9].

Because the accelerating gradient scales with plasma density, substantially higher fields may be achieved using solid-state plasmas, whose electron densities (10^{22}–10^{24} cm^{-3}) are approximately three orders of magnitude greater than those of conventional gaseous plasmas. In principle, this increase could enable accelerating gradients approaching the TeV/m regime. This concept was demonstrated in numerical studies by Bonţoiu et al. [10, 11], where particle-in-cell (PIC) simulations showed that solid-state targets composed of carbon nanotube (CNT) bundles can serve as an effective medium for accelerating self-injected electrons within a laser-driven wakefield bubble, analogous to the blowout regime of LWFA in gaseous plasmas.

In a recent study [11], Bonţoiu et al. employed the PICon-GPU code [12] to demonstrate that a three-cycle, 800-nm, circularly polarized laser pulse with a peak power of 35.5 TW can generate a relativistic electron bunch in a CNT bundle target. Motivated by those results, we perform analogous fully three-dimensional PIC simulations using the WarpX v. 25.10 code [13]. Here, we directly compare the electron beam properties obtained with linearly and circularly polarized laser pulses interacting with the same CNT bundle target, aiming to assess the influence of laser polarization on the acceleration process.

THE MODEL

The 3D-WarpX simulations were carried out on the SDumont supercomputing cluster, using 16 NVIDIA Volta V100 GPUs (32 GB each). The physical system consists of an 800 nm wavelength laser pulse propagating along the z-axis through a CNT bundle target whose longitudinal direction is aligned with the laser propagation axis. The laser is modeled by a few-cycle Gaussian temporal and transverse profile [14]. Two simulations were performed, differing only in the laser polarization: linear polarization along the y direction and circular polarization.

The computational domain extends from $-3.5 \leq z \leq 27.5$ µm longitudinally and -3.5 µm $\leq x, y \leq 3.5$ µm transversely, with $N_{x,y,z} = 1024$ cells in each direction. Each cell is initialized with $N_{\mathrm{PPC}} = 8$ macroparticles ($2 \times 2 \times 2$). The timestep is set to 0.999, CFL, where CFL denotes the Courant–Friedrichs–Lewy stability limit, and the simulations are run for $N_{\mathrm{step}} = 5250$ time steps. The laser parameters are $a_0 = 21.6$, $\lambda_0 = 800$ nm, $w_0 = 1.5$ µm, pulse duration $\tau = 2.67$ fs (FWHM in intensity), peak intensity $I_0 = 10^{21}$ W/cm^2, and pulse energy $E = 100$ mJ.

The target geometry reproduces that described in Ref. [11], although the present simulations employ higher spatial resolution and a larger number of particles per cell. The target consists of CNT bundles modeled as initially neutral solid

* This study was financed in part by the Conselho Nacional de Desenvolvimento Cientifico e Tecnológico (CNPq, Grants 405143/2021-4 and 140941/2023-1), by the Fundação de Amparo à Pesquisa do Estado do Rio Grande do Sul (FAPERGS, Grant 24/2551-0001552-3), and by the Coordenação de Aperfeiçoamento de Pessoal de Nível Superior - Brasil (CAPES) - Finance Code 001.
† brunosnunes@usp.br

carbon cylinders with radius $r_b = 12.5$ nm and density $n_b = 10^{22}$ cm^{-3}. The bundles are arranged along concentric cylindrical shells that serve as immaterial geometric guides for their spatial distribution. For each shell, the number of bundles and their angular separation are chosen to maintain a constant effective density along the circumference, with positions determined from a random initial phase angle. This procedure yields an overall effective density [15] of $n_{\text{eff}} = 3 \times 10^{20}$ cm^{-3}. A central aperture with inner radius $r_{in} = 0.5$ µm is included to allow propagation of the laser core through the target. Despite representing the same physical system, different postprocessing approaches prevent direct comparison between the results of this work and those reported in Ref. [11]. In the previous work, beam properties were computed from particles trapped within the wakefield bubble volume. Here, we consider all particles exiting the target whose longitudinal momentum corresponds to kinetic energies exceeding 20 MeV, under the assumption that the particle energy is predominantly longitudinal.

RESULTS

Following the mechanism described in Ref. [11], the laser pulse ionizes the CNT target and drives electrons toward the outer shells of the structure. This leads to the formation of a propagating wakefield bubble, closely resembling the wake structures observed in laser wakefield acceleration (LWFA) in gas-jet targets. Electrons are self-injected at the rear of the bubble, where they experience longitudinal electric fields on the order of TV/m.

This process is illustrated in the simulation snapshots shown in Fig. 1 (a–f), which depict an approximately 4, µm-wide wakefield bubble propagating inside the target. The left panels—(a), (c), and (e)—display the longitudinal electric field (E_y) at the center of the bubble using a blue–white–red color scale for circular laser polarization, while the right panels show the corresponding field for linear polarization. The wakefield bubble contains an electron bunch whose kinetic energy is represented by a yellow–orange–purple–black color scale, applied only to backtracked electrons that satisfy the selection criteria. These electrons are self-injected at the rear of the bubble and subsequently accelerated. The gray lines indicate the positions of a subset of CNT bundles and are included solely to illustrate the target geometry. Black contour lines represent the laser intensity.

Overall, the wakefield structures in the left and right panels are very similar, with only minor discrepancies observed behind the bubble rear in panels (c) and (d), and more noticeably in panels (e) and (f). In the latter case, panel (e) exhibits a stronger positive electric field in the region $12.5 < z < 15$ µm compared to panel (f). Furthermore, in addition to the field discrepancies, small differences are also observed in the accelerated particles. The left-column panels show a small number of particles being accelerated within a weakly defined second wakefield bubble, which is not present in the right-column panels.

Table 1: Bunch parameters at extraction

Parameter	Circular	Linear
Total charge, Q [pC]	493	448
Average energy, $\bar{E}$ [MeV]	38.7	37.0
Energy spread (RMS), σ_E [MeV]	9.3	8.7
Average acceleration gradient, $\bar{A}$ [TeV/m]	2.6	2.5
Bunch longitudinal length (FWHM), Δz [µm]	1.0	1.3
Bunch transverse size (FWHM), Δx; Δy [µm]	1.8	1.7
Normalized horizontal emittance (RMS), ϵ_x [µm rad]	2.64	2.65
Horizontal divergence (FWHM), Θ_x [mrad]	79.0	77.1
Normalized vertical emittance (RMS), ϵ_y [µm rad]	2.51	2.51
Vertical divergence (FWHM), Θ_y [mrad]	77.8	84.0

The properties of the extracted bunch are shown in Fig. 1(g–n), arranged in two rows, circular polarization on top and linear polarization below, to allow direct visual comparison. All eight panels share the same density color scale. Panels (g,h) and (k,l) present the transverse phase spaces. In the circular case, the beam exhibits divergences up to $\sim$ 0.4 rad and a slight displacement from the target axis, whereas the linear case shows a more centered distribution with particles preferentially aligned along a nearly diagonal structure.

The longitudinal phase spaces (i,m) indicate bunch lengths of approximately 1 µm for both polarizations; however, the linear case displays a distinct V-shaped feature for particles beyond 17 µm that is absent under circular polarization. The transverse spatial distributions (j,n) further highlight different symmetry properties: circular polarization yields a comparatively homogeneous density, with a mild concentration in the quadrant $x < 0$ µm, $y > 0$ µm, while linear polarization produces a clear asymmetry along the y-axis, with a larger fraction of particles located at $y < 0$ µm.

Figure 2 presents the electron energy spectra for circular (blue) and linear (red) polarization. The two spectra are highly similar, extending from the selection threshold at 20 MeV up to nearly 60 MeV and exhibiting a well-defined quasi-monoenergetic peak in both cases. The peak energy is slightly higher for circular polarization (45.4 MeV) than for linear polarization (43.0 MeV). Despite their nearly identical spectral profiles, the bunch produced with circular polarization carries a higher total charge, with an increase of approximately 45 pC (~9%) relative to the linear case.

A quantitative comparison of the extracted beam parameters is summarized in Table 1. Apart from the total charge, both polarization states yield very similar beam properties, with only minor variations in average energy, RMS energy

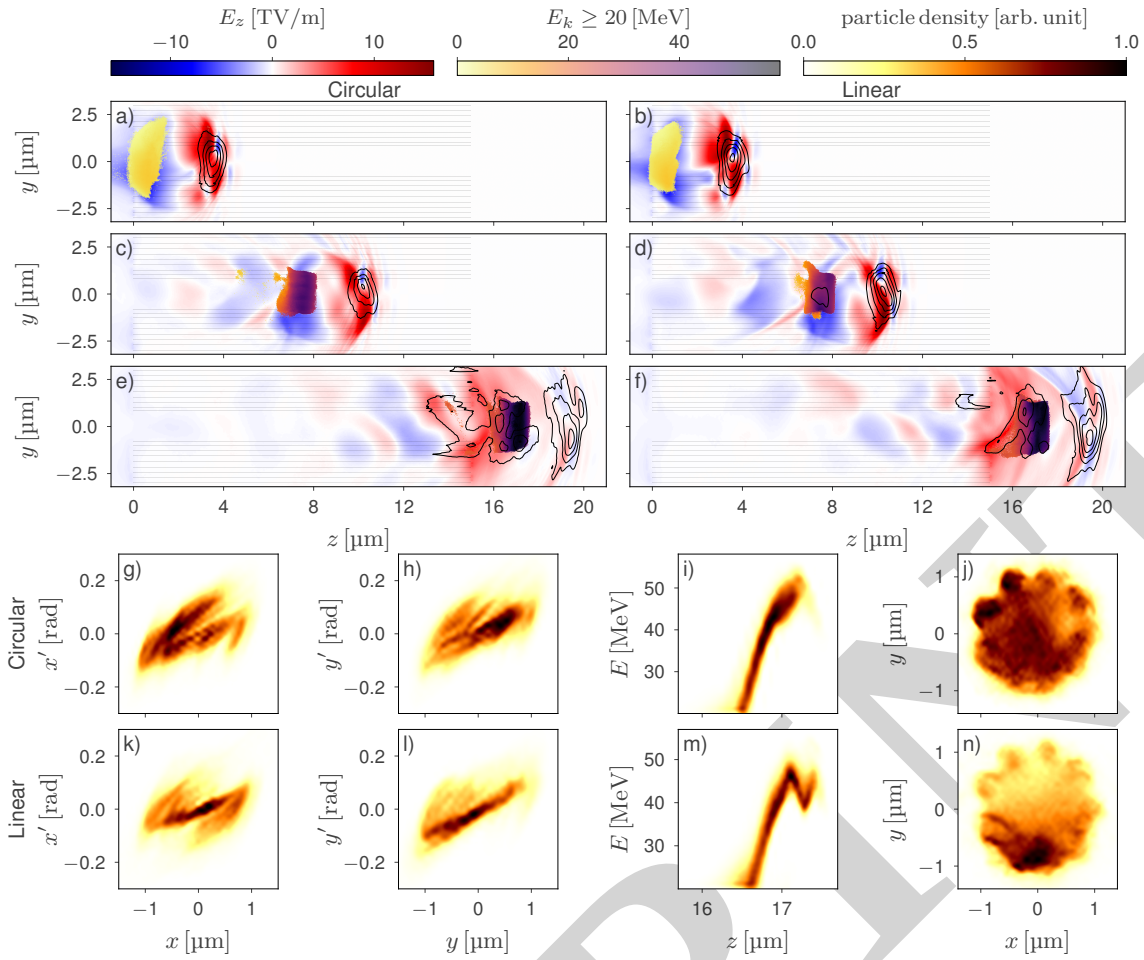

Figure 1: Panels (a–f) show different propagation stages of the longitudinal electric field (E_y, blue–white–red colormap) and accelerated electron macroparticles (yellow–orange–purple–black colormap) in a CNT target with effective density $n_e \simeq 3 \times 10^{20}$ cm^{-3}, with circular polarization in the left column and linear polarization in the right. Gray lines indicate selected CNT bundles, and black contours denote the laser intensity. Panels (g–n) present the extracted bunch properties: circular polarization in the upper row and linear polarization in the lower row, including transverse phase spaces (g,h,k,l), longitudinal phase spaces (i,m), and transverse spatial distributions (j,n).

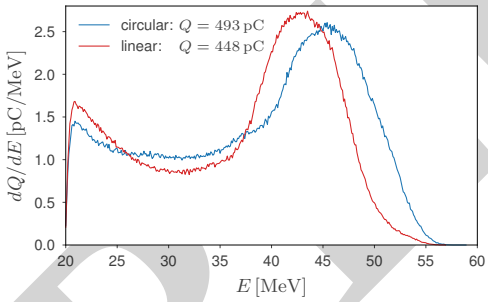

Figure 2: Comparison of the two electron energy spectra.

spread, acceleration gradient, bunch dimensions, emittance, and divergence.

CONCLUSION

The use of circular or linear laser polarization in a CNT target leads to the generation of electron bunches with comparable overall characteristics. Circular polarization increases the charge of electrons above 20 MeV by approximately 9%, while differences in average energy, energy spread, emittance, divergence, and other beam parameters remain below 5%. These results indicate that laser polarization primarily affects the self-injection efficiency and resulting charge, with minimal impact on the intrinsic beam quality.

ACKNOWLEDGEMENTS

The authors acknowledge computing resources provided by LNCC's SDumont HPC system (project LPA-FARMA).

REFERENCES

[1] E. Esarey, C. B. Schroeder, and W. P. Leemans, "Physics of laser-driven plasma-based electron accelerators," *Rev. Mod. Phys.*, vol. 81, no. 3, pp. 1229–1285, 2009. doi:10.1103/RevModPhys.81.1229

[2] T. Tajima, and J. M. Dawson, "Laser Electron Accelerator," *Phys. Rev. Lett.*, vol. 43, no. 4, pp. 267–270, 1979. doi:10.1103/PhysRevLett.43.267

[3] S. P. D. Mangles, C. D. Murphy, Z. Najmudin, *et al.* "Monoenergetic beams of relativistic electrons from intense laser–plasma interactions," *Nature*, vol. 431, no. 7008, pp. 535–538, 2004. doi:10.1038/nature02939

[4] P. Chen, J. J. Su, J. M. Dawson, *et al.* "Energy Transfer in the Plasma Wake-Field Accelerator," *Phys. Rev. Lett.*, vol. 56, no. 12, pp. 1252-1255, 1986. doi:10.1103/PhysRevLett.56.1252

[5] B. S. Nunes, S. P. Santos, R. P. Nunes, *et al.* "Bayesian optimization of laser wakefield acceleration in the self-modulated regime (SM-LWFA) aiming to produce molybdenum-99 via photonuclear reactions," *Phys. Plasmas*, vol. 32, no. 3, pp. 033101, 2025. doi:10.1063/5.0244268

[6] L. Labate, D. Palla, D. Panetta, *et al.* "Toward an effective use of laser-driven very high energy electrons for radiotherapy: Feasibility assessment of multi-field and intensity modulation irradiation schemes," *Sci. Rep.*, vol. 10, no. 1, pp. 17307, 2020. doi:10.1038/s41598-020-74256-w

[7] R. W. Assmann, M. K. Weikum, T. Akhter, *et al.* "EuPRAXIA Conceptual Design Report," *Eur. Phys. J. Spec. Top.*, vol. 229, no. 24, pp. 3675–4284, 2020. doi:10.1140/epjst/e2020-000127-8

[8] C. B. Schroeder, E. Esarey, C. G. R. Geddes, *et al.* "Physics considerations for laser-plasma linear colliders," *Phys. Rev. ST Accel. Beams*, vol. 13, no. 10, pp. 101301, 2010. doi:10.1103/PhysRevSTAB.13.101301

[9] C. B. Schroeder, C. Benedetti, E. Esarey, *et al.* "Laser-plasma-based linear collider using hollow plasma channels," *Nucl. Instrum. Methods Phys. Res., Sect. A*, vol. 829, pp. 113–116, 2016. doi:10.1016/j.nima.2016.03.001

[10] C. Bonţoiu, Ö. Apsimon, E. Kukstas, *et al.* "Author Correction: TeV/m catapult acceleration of electrons in graphene layers," *Sci. Rep.*, vol. 13, pp. 2845, 2023. doi:10.1038/s41598-023-29761-z

[11] C. Bonţoiu, A. Bonatto, Ö. Apsimon, *et al.* "Numerical study of self-injected electron acceleration in CNT structured targets driven by an 800 nm laser," *Sci. Rep.*, vol. 15, no. 1, pp. 45323, 2025. doi:10.1038/s41598-025-29386-4

[12] H. Burau, R. Widera, W. Hönig, *et al.* "PIConGPU: A Fully Relativistic Particle-in-Cell Code for a GPU Cluster," *IEEE T. Plasma Sci.*, vol. 38, no. 10, pp. 2831-2839, 2010. doi:10.1109/TPS.2010.2064310

[13] J.-L. Vay, M. Acciarri, A. Almgren, *et al.* "BLAST-WarpX/warpx: 26.02 (26.02)" *Zenodo*, 2026. doi:10.5281/zenodo.18475787

[14] C. F. R. Caron and R. M. Potvliege, "Free-space propagation of ultrashort pulses: Space-time couplings in Gaussian pulse beams," *J. Mod. Opt.*, vol. 46, no. 13, pp. 1881–1891, 1999. doi:10.1080/09500349908231378

[15] A. Bonatto, G. Xia, O. Apsimon, *et al.* "Exploring ultra-high-intensity wakefields in carbon nanotube arrays: An effective plasma-density approach," *Phys. Plasmas*, vol. 30, no. 3, pp. 033105, 2023. doi:10.1063/5.0134960